

Multiwall carbon nanotube microcavity arrays

Rajib Ahmed,¹ Ahmmmed A. Rifat,² Ali K. Yetisen,^{3,4} Qing Dai,⁵ Seok Hyun Yun,^{3,4} and Haider Butt^{1,a)}

¹*Nanotechnology Laboratory, School of Mechanical Engineering, University of Birmingham, Birmingham B15 2TT, United Kingdom*

²*Integrated Lightwave Research Group, Department of Electrical Engineering, Faculty of Engineering, University of Malaya, Kuala Lumpur 50603, Malaysia*

³*Harvard Medical School and Wellman Center for Photomedicine, Massachusetts General Hospital, 65 Landsdowne Street, Cambridge, Massachusetts 02139, USA*

⁴*Harvard-MIT Division of Health Sciences and Technology, Massachusetts Institute of Technology, Cambridge, Massachusetts 02139, USA*

⁵*National Center for Nanoscience and Technology, Beijing 100190, China*

(Received 28 October 2015; accepted 3 March 2016; published online 16 March 2016)

Periodic highly dense multi-wall carbon nanotube (MWCNT) arrays can act as photonic materials exhibiting band gaps in the visible regime and beyond terahertz range. MWCNT arrays in square arrangement for nanoscale lattice constants can be configured as a microcavity with predictable resonance frequencies. Here, computational analyses of compact square microcavities ($\approx 0.8 \times 0.8 \mu\text{m}^2$) in MWCNT arrays were demonstrated to obtain enhanced quality factors (≈ 170 – 180) and narrow-band resonance peaks. Cavity resonances were rationally designed and optimized (nanotube geometry and cavity size) with finite element method. Series (1×2 and 1×3) and parallel (2×1 and 3×1) combinations of microcavities were modeled and resonance modes were analyzed. Higher order MWCNT microcavities showed enhanced resonance modes, which were red shifted with increasing Q-factors. Parallel microcavity geometries were also optimized to obtain narrow-band tunable filtering in low-loss communication windows (810, 1336, and 1558 nm). Compact series and parallel MWCNT microcavity arrays may have applications in optical filters and miniaturized optical communication devices. © 2016 AIP Publishing LLC. [<http://dx.doi.org/10.1063/1.4944318>]

I. INTRODUCTION

Multi-wall carbon nanotubes (MWCNTs) are multiple layers of graphene rolled into a tubular form.¹ They have a unique set of mechanical, electronic, and optical properties^{2–4} exhibiting strong anisotropic nonlinearity.^{5–7} MWCNTs absorb the total optical spectrum in ultra-fast lasers, bolometric detectors, and photonic crystals.^{8,9} They are generally metal and able to carry high surface current density for application such as field emission/rectifier displays, solar cells, optical antennas, and inter-connections.^{8,10,11} Optical properties of the nanotubes were also used in polymeric optical fibers, passive mode-locked lasers, ultrafast optical switching, polarization rotators, and four-wave-mixing.^{12–14} MWCNTs have been nanofabricated using plasma-enhanced chemical vapor deposition (PECVD) (tube diameter = 1–2 nm) to produce arrays on predetermined locations, orientation, and lengths.^{8,15,16}

Periodic MWCNT arrays with a lattice constant on the order of 100 nm exhibit photonic band-gap effects in the optical and terahertz regimes, analogous to 2D photonic crystal arrays.¹⁷ The periodic MWCNTs show diffraction and resonance when the periodicity matches the incident light wavelength. The geometry (radius or spacing) variation determines the resonance wavelength depending on the filling factor.¹⁸ Moreover, the periodic MWCNTs composed of

warped graphite sheets allow fast electron transport. Therefore, different resonance frequencies can be achieved with periodic MWCNT arrays.¹⁹ Periodic MWCNT arrays were reported to have waveguide effect that filters wavelengths at 850 and 1550 nm.¹⁷ The waveguide effect was due to the photonic bandgap in the nanotube arrays containing line defects. The line defects in MWCNTs showed stop-band and pass-band with the incident light analogous to a photonic crystal waveguide. Similar effects were created in MWCNTs in square arrays, which acted as a light absorber to trap light and have microresonance operation.

We have previously demonstrated computational modeling and fabrication of periodic MWCNT arrays as optical devices. Periodic array of MWCNTs was arranged to show negative index as diffractive photonic crystal lenses in planar, convex, and concave configurations.¹⁰ These periodic MWCNTs could be used to create a CNT waveguide.¹⁷ MWCNTs also showed cutoff resonance to electromagnetic waves and filtered light at near-infrared region (1500 nm).²⁰ Additionally, we modeled MWCNTs to demonstrate an application in optical filtering.¹⁹ Recently, we demonstrated that periodic MWCNTs could be utilized as negative index materials in biconvex configuration.¹⁸

Here, we demonstrate finite element-based computational analyses of periodic MWCNT arrangements having 50 nm radius and 400 nm lattice spacing in square arrays that act as a microcavity. The effect of cavity geometry on the

^{a)}Email: h.butt@bham.ac.uk. Tel.: +441214158623.

transmitted spectra was modeled to predict the optical characteristics. The concept of series and parallel MWCNT microcavity was introduced for the first time to obtain narrow-band peaks at longer resonance wavelengths. Here, basic MWCNT arrays were considered into larger array assemblies for enhanced optical control, and that series and parallel geometries with respect to the incident light. The MWCNT microcavities allowed filtering out wavelengths at low-loss communication windows (810, 1336, and 1558 nm). MWCNT microcavities displayed improved Q-factor resonances and resonance tuning based on their geometry.

II. MODELING OF MWCNT MICROCAVITIES

The dielectric property of the CNTs was modeled with Drude–Lorentz model as a function of operating wavelength for the p -polarized light (TE field), which was incident to the longitudinal direction (z -axis) of CNTs.¹⁹ The optical properties of anisotropically dense MWCNT arrays are comparable to bulk graphene^{21,22} and they act as dielectric metamaterials.²⁰ MWCNTs are highly anisotropic due to dielectric response functions, and $\epsilon_{\perp}(\omega)$ and $\epsilon_{\parallel}(\omega)$, respectively, depending on the parallel and perpendicular electric field on c -axis (symmetric axis of CNTs).⁸ The dielectric function of MWCNT for Drude–Lorentz model (p -polarized light) is

$$\epsilon_{\perp}(\omega) = 1 - \underbrace{\frac{\omega_p^2}{\omega^2 + i\frac{\omega}{\tau}}}_{\text{Intra_band_effects}} + \underbrace{\sum_{m=1}^M \frac{\omega_p^2}{\omega_m^2 - \omega^2 + i\omega\gamma_m}}_{\text{Intra_band_effects}}, \quad (1)$$

where ω_p is the free electron plasma frequency and τ is the relaxation time.¹⁹ The first term (Drude) indicates intraband effects due to the free electrons within CNTs. The last term of the dielectric function is due to interband effects due to bounded electrons described with modified Lorentz model. This model assigns oscillators to the critical points in the joint density of states. The absorption between the critical points results in interband transition of the modeled oscillators with energy, $\hbar\omega_m$, strength, σ_m , damping constraint, γ_m , and frequency, ω_m . In Eq. (1), Lorentz part representing the plasmonic resonance plays a role in the visible regime, while the Drude part represents free carrier localization and cannot be neglected at the high frequency regime.^{17,19,23} The dielectric function of model MWCNT using $M=7$ shows a good fit with experimental data.⁸ These model parameters were used to define the MWCNT dielectric constant for the optical and infrared (IR) regimes.¹⁹

A 2D geometry was computed for the simulation simplicity, and the electric field was invariant along the z -axis of CNTs. The heights of CNTs were several times larger and their widths were smaller than the operating wavelength. This ensured high optical contrast between the CNTs and dielectric matrix; therefore, periodic arrangement of CNTs would act as wire-metamaterials and their property would depend on plasmonic resonance.¹⁷ The wavelength dependent dielectric constant of the MWCNT was modeled within the optical and IR regime with Drude–Lorentz model, and

incorporated in the simulation with the polynomial curve fitting, $E_{\perp}(\omega) = \text{Re}(E_{\perp}(\omega)) + \text{Im}(E_{\perp}(\omega)) * j$, where $\text{Re}(E_{\perp}(\omega))$ and $\text{Im}(E_{\perp}(\omega))$ represent real and imaginary parts of the polynomial. The coefficients of the polynomials were used as variables in COMSOL Multiphysics software. The real and imaginary parts of the MWCNT dielectric constants were incorporated into the simulation as a function of the frequency.¹⁹ COMSOL Multiphysics is based on the finite element method (FEM).^{24–26} The scattering boundary conditions were used to contain the MWCNTs in a square geometry, and continuity boundary condition was used for the MWCNTs.¹⁸ The computational area was meshed by the triangular domain elements and maximum element size was $\lambda/5$. The minimum number of degrees of freedom was 30 331 with a solution time of 322.896 s. Convergence test was carried out to optimize computational mesh size ($\lambda/5$) to improve the simulation accuracy.^{27,28}

The microcavity was modeled by the periodic arrangement (spacing $a=400$ nm and radius $R=50$ nm) of MWCNTs with square arrangement (Fig. 1(a)).¹⁸ MWCNTs were arranged as a square block ($m \times n$ matrix arrays) without a central MWCNT that acted as a resonant cavity. Three rows and columns with different MWCNT dimensions (1st, 3rd, and 2nd rows having radius R and R_1 , respectively) were designed to have periodic spacing (a) between nanotubes. The spacing and radius between the MWCNTs were $a=400$ nm and $R=R_1=45$ nm, which provided the cavity an 800 nm wide base.

The transmission spectrum showed narrow-band resonant modes at 685 nm (λ_1) (Fig. 1(b)). Another narrow-band resonance was found at 450 nm (λ_2). A low-intensity peak was also observed at 150 nm (λ_2), but it did not resonate the cavity. The resonance of the cavity depended on the band-gap effect of periodic MWCNTs. Strong resonance frequency of the cavity was comparable to cavity size.¹⁸ In this configuration, MWCNT-cavity showed a Q factor of ~ 172 . The Q factor of the MWCNT cavity depends on the bandwidth of the resonance peak

$$Q \text{ factor} = \frac{f_{res}}{\Delta f_{FWHM}}, \quad (2)$$

where f_{res} is the resonance frequency of the cavity and Δf_{FWHM} is the full-width at half-maximum bandwidth at resonance frequency. Decreasing the cavity spacing of periodic MWCNT arrangement would increase resonance bandwidth and decrease the Q-factor. The narrow-band resonance was achieved due to large cavity size (Fig. 1(a)). Based on the demonstrated model that predicted the resonance properties and transmission spectra, the structure of microcavity can be optimized for high Q factors and desired resonance frequencies.

III. OPTIMIZATION OF MWCNT MICROCAVITY

MWCNT cavities behave like a Fabry–Perot cavity, and their resonance mode depends on the geometry and dimension. Therefore, an analysis has been performed to understand the dependency of the resonance mode on nanotube radius (R and R_1), spacing (a), or cavity size. CNT radius in

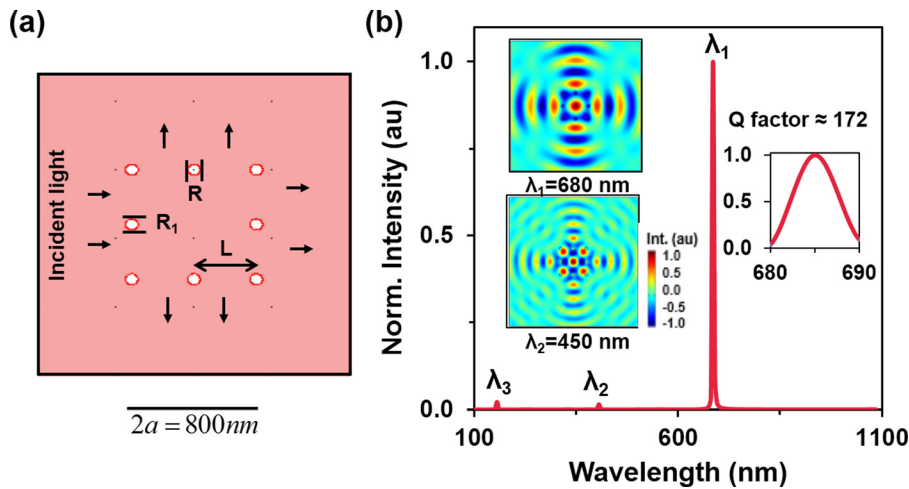


FIG. 1. FEM model of MWCNT microcavity arrays. (a) The geometry of a microcavity designed with periodic square arrangement. (b) Normalized transmission intensity of the microcavity shown in (a). The inset shows resonance wavelength and Q factor.

the first and third cavity rows was termed as R, while the CNT radius in the second (middle) row was termed as R_1 .

A. Nanotube geometry optimization

As the radii of MWCNTs ($R = R_1$) were increased, the resonance peak shifted to shorter wavelengths (Fig. 2(a)). The resonance peak, which was originally at 735 nm for $R = R_1 = 30$ nm, shifted to 700 and 665 nm when $R = R_1$ was increased from 42 to 50 nm, respectively. This resonance shift was due to the increase in fill-factor depending on radius increase, which reduced the empty space within the cavity. As the radii of MWCNTs were increased ($R = R_1$), the

resonance peak shifted to shorter wavelengths (Figs. 2(a) and 2(b)), which could be due to the intensity distribution for the extra side lobes (small resonance peaks). The number of side lobes was increased as the radius increased. Hence, the intensity and band of the resonance peak depended on the radii of MWCNTs. Similar results were also found with MWCNT radii change in the second rows (R_1) of square MWCNT cavity, as the radii of the first and third rows were kept constant ($R = 50$ nm) (Figs. 2(c) and 2(d)).

With increasing radius, main peaks shifted to shorter wavelengths, but side lobe peaks remained in the same positions and their intensity decreased (inset in Fig. 2(c)). This phenomenon can be seen from the side lobes. In both cases,

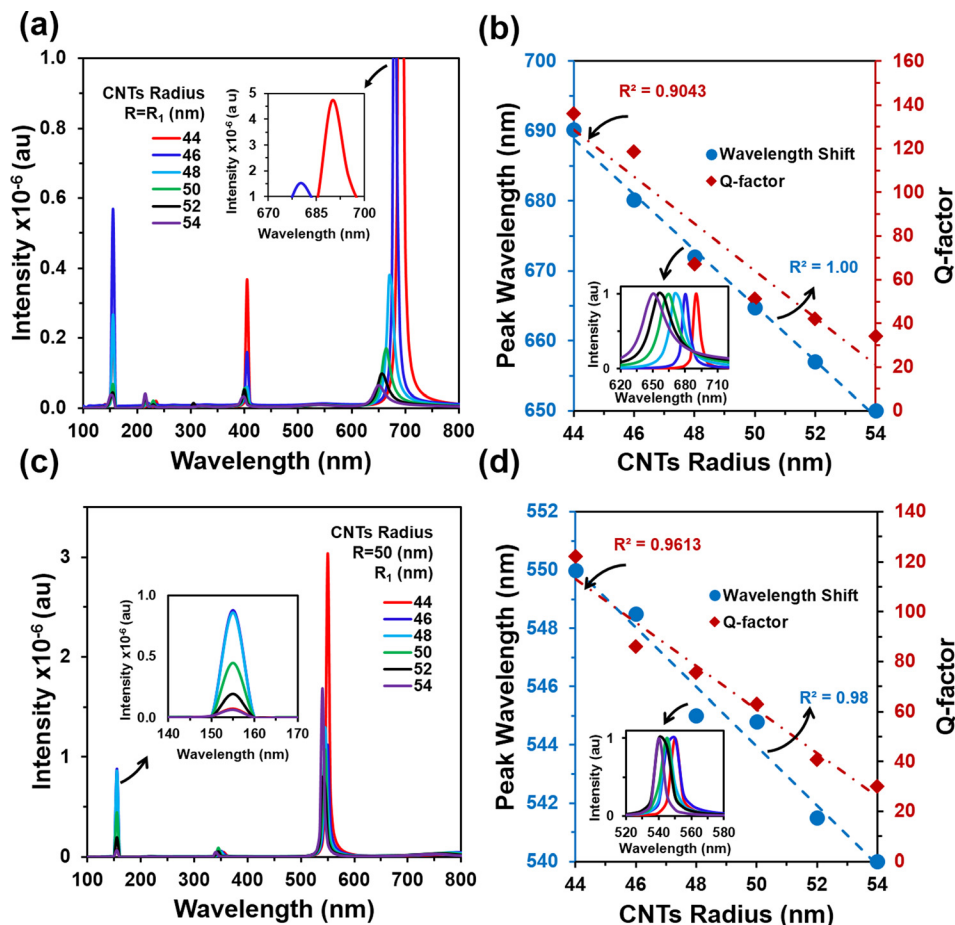


FIG. 2. Optimization of MWCNT microcavities. (a) Normalized transmission intensity as a function of nanotube radius ($R = R_1$). The inset shows the magnified peaks. (b) The linear fit curve for the resonance peak shift and the Q factor as a function of nanotube radius ($R = R_1$). Inset shows the resonance wavelength blue shift and bandwidth increases as the radius increases. (c) Normalized transmission intensity with varying nanotube radius (R_1) with constant R . The inset shows the magnified peaks for the resonance peak shift and the Q factor as a function of nanotube radius ($R = 50$ nm, R_1 increases). Inset shows the resonance wavelength blue shift and bandwidth increases as the radius increases.

the resonance frequency of the microcavity shifted to the shorter wavelengths as the MWCNT radii was increased. This is due to the filling factor increase, as MWCNTs radius increased and decreased in empty space within the cavity.¹⁸ Similarly, the Q-factor values decreased as the radius was increased. Therefore, a small radius of MWCNTs is desired for higher wavelength shift and narrow-band peaks, but this is a trade-off between fabrication complexity and quality.

B. Cavity size optimization

A microcavity was designed with MWCNT spacing of $a = 400$ nm, and the lattice constant was varied to expand or contract the microcavity internal size, $L = a$. Peak resonance shifted to longer wavelengths with expanding lattice spacing or increasing cavity size. The resonance peaks were originally at 350 nm and 595 nm for $a = 400$ nm. These peaks shifted to 425 nm and 730 nm for $a = 420$ nm; and shifted to 460 nm and 795 nm for $a = 450$ nm, respectively (Fig. 3(a)). Figure 3(b) shows microcavities at their resonance modes. For $a = 450$ nm, more resonance modes were observed due to having more spacing within the cavity. However, a narrow-band resonance was observed for $a = 400$ and

420 nm MWCNT cavity. A higher Q factor (≈ 171) was found for $a = 400$ nm cavity size, even their FWHM bandwidth was almost the same (≈ 4 nm) due to high resonance value ($\lambda_{\text{res}} \approx 685$ nm). For large cavity sizes, such as $a = 450$ nm, longer resonance values were found, but Q-factor value remained small due to broader FWHM bandwidth.

The red shift of the resonance peak was found with expanding lattice spacing (L). This can be attributed to the decrease in fill factor due to increasing CNT lattice spacing (L). For lower cavity sizes, lower resonance intensities were observed, which could be due to the intensity distribution to the side lobes at smaller resonance wavelengths. The number of resonant modes was increased due to enlarged spacing within the cavity. Moreover, by varying the cavity size, the resonance frequency and Q-factor could be tuned.¹⁸

IV. SERIES AND PARALLEL MWCNT MICROCAVITIES

MWCNT cavities were arranged in series and parallel configurations with respect to the input light for analyzing resonance peaks. MWCNT radius and cavity spacing were configured to act as series (1×2 and 1×3) or parallel (2×1

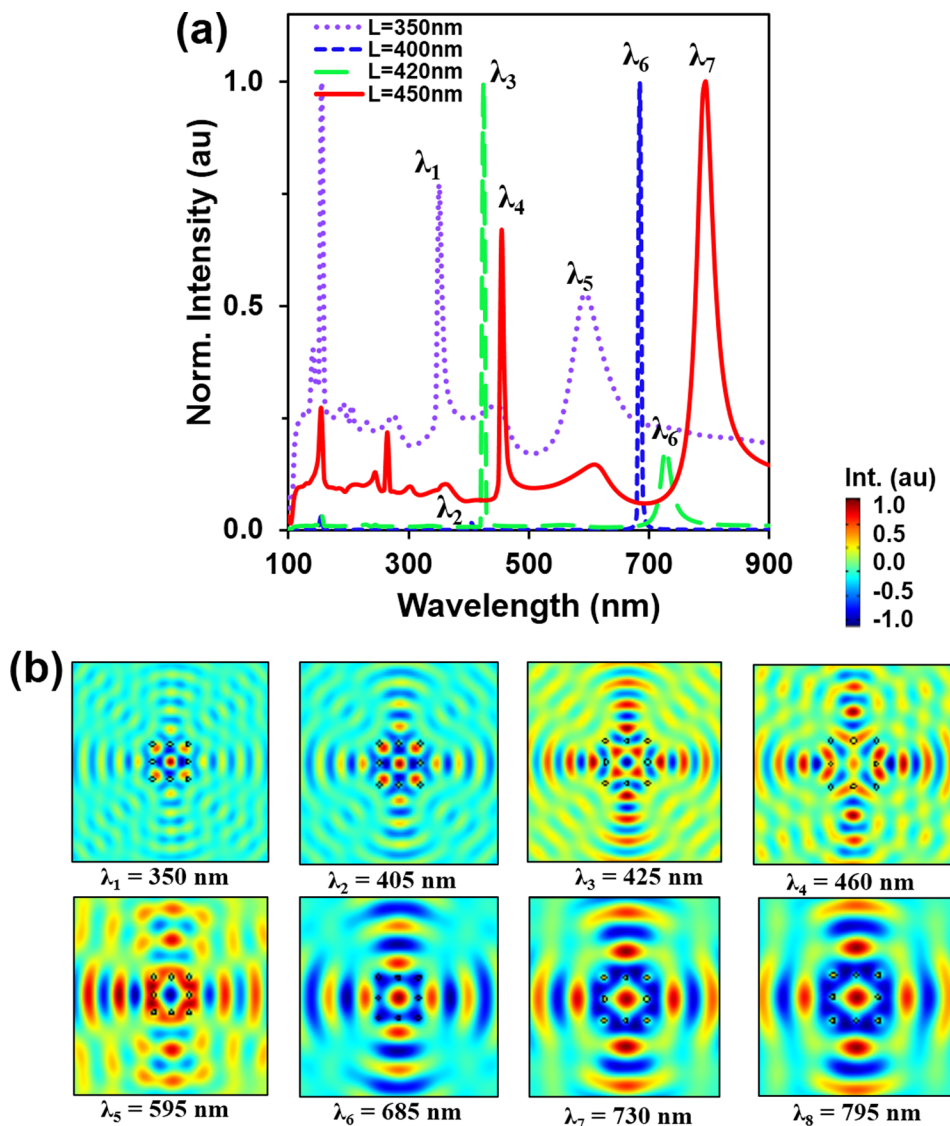


FIG. 3. Lattice spacing optimization of MWCNT microcavities. (a) Normalized transmission intensity through square microcavity configuration as a function of variation in nanotube spacing ($L = a$). (b) Magnified microcavities at their resonance modes for the peaks shown in (a).

and 3×1) resonators. Figure 4 shows the peaks of the series resonators and parallel resonator with optimized parameters (1st resonator, $R = 50$ nm, $R_1 = 40$ nm and 2nd resonator, $R = 40$ nm and $R_1 = 30$ nm; cavity separation $2a(800$ nm)). Resonance frequency shifted to longer wavelengths as the number of cavities was increased. The resonance maxima were at 570 nm for a 1×2 series resonator, and this peak shifted to 680 nm for a 1×3 series resonator (Fig. 4(a)). Figure 4(c) shows the resonance modes for series microcavities. The number of resonance peaks also increased with higher order resonator having narrow-band resonance peaks. Therefore, Q factor value (≈ 155) for 1×3 array was 1.5 times higher than 1×2 resonators. Additionally, the bandwidth of the peaks also increased with cavity separation.

Parallel configuration of the microcavities also showed narrow-band resonance peaks. The resonance peaks were at 660 and 830 nm for 2×1 and 3×1 configurations, respectively (Fig. 4(b)), and lower resonance peaks also existed for higher orders (3×1) analogous to series resonators but intensity was lower. Figure 4(d) shows the resonance modes for parallel microcavities. As the number of parallel resonators increased, the resonance peaks become narrower and shifted to longer wavelengths. This optical phenomenon was found in both series and parallel resonators. The Q factor values also increased for the parallel microcavity at higher orders due to narrow-band peaks at longer resonance wavelengths. The Q-factor (≈ 150) of 3×1 parallel resonator was

1.7 times higher than 2×1 configuration. Compared with the series resonators, parallel resonators have resonance peaks at longer wavelengths.

Further analyses have been performed to use MWCNT series and parallel configurations for tunable wavelength filtering. Figure 5(a) shows a 2×1 parallel MWCNT cavity arrangement for wavelength filtering at low loss communication windows. MWCNT radii for the 1st and 3rd rows were assigned as $R = 50$ nm for upper and lower cavities. MWCNT radii of 2nd row, R_1 (50 nm), for lower cavity was kept constant but R_1 for upper cavity was varied from 30, 50, to 60 nm to filter light at 1335, 810, and 1558 nm, respectively.

Figure 5(c) shows the resonance modes for the low loss communication windows. MWCNT radius and lattice spacing were optimized to filter light at low loss communication windows with a single parallel MWCNT microcavity (Fig. 5(b)). For $\lambda \geq 1400$ nm, lower cavity resonance was at 1558 nm; for $850 \text{ nm} \leq \lambda \leq 1400$ nm, upper cavity resonance was at 1336 nm; and for $\lambda \leq 450$ nm, upper and lower cavity partial resonance occurred at 840 nm.

V. DISCUSSION

Our computational modeling of periodic MWCNT suggested that narrow-band resonance with improved Q-factor could be realized with series and parallel MWCNT microcavity arrays. The parallel MWCNT array showed tunable

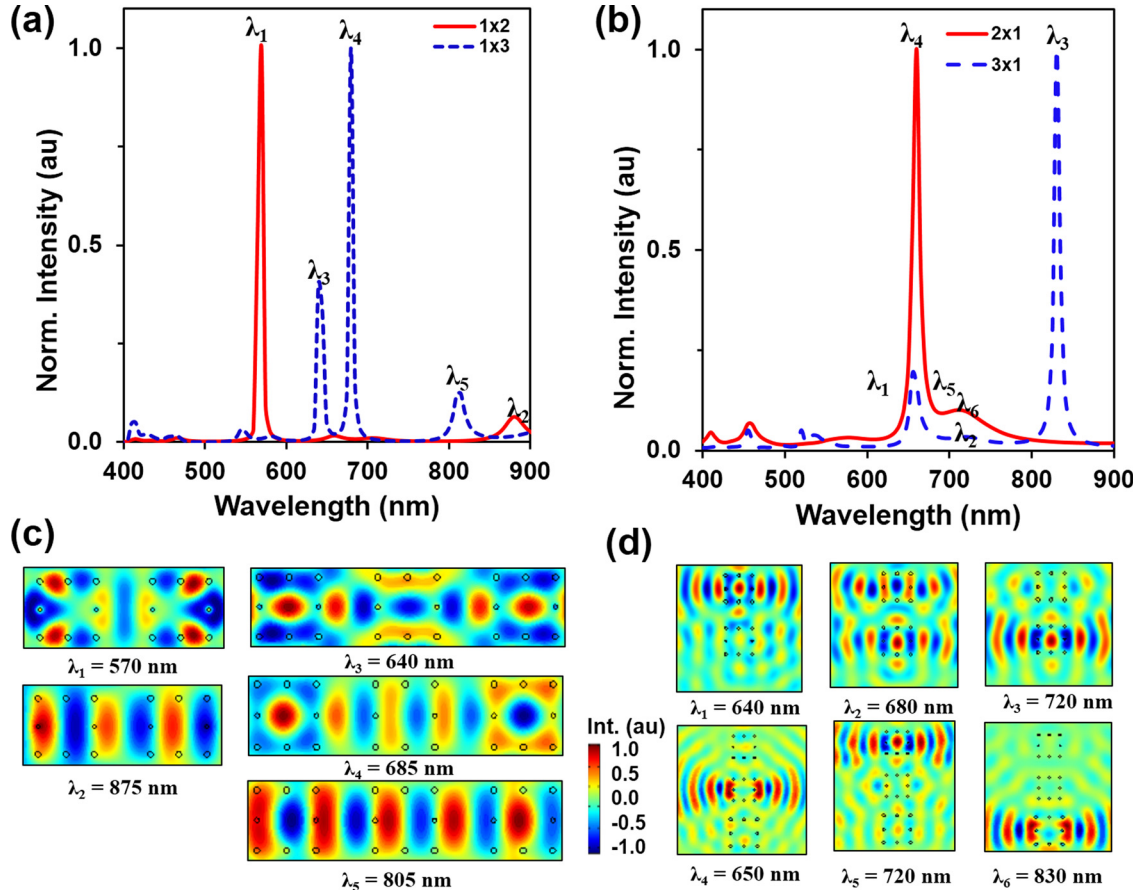


FIG. 4. Series and parallel MWCNT microcavities. Normalized transmission intensity in (a) series (1×2 and 1×3) and (b) parallel (2×1 and 3×1) resonator configurations. (c) Series and (d) parallel microcavities at their resonance modes for the peaks shown in (a) and (b).

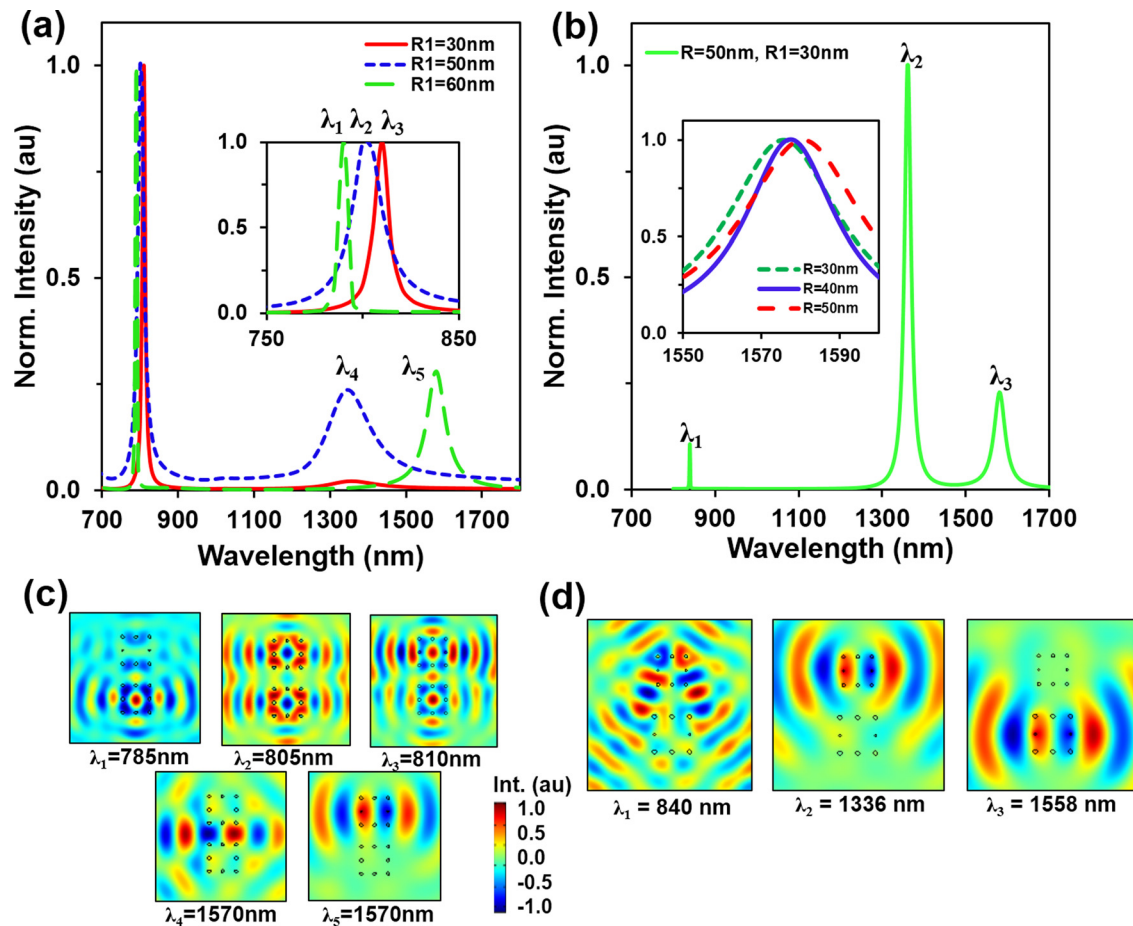


FIG. 5. Square MWCNT microcavities as tunable filters. Normalized transmission intensity for (a) 2×1 and (b) 3×1 parallel microcavities as a function of variation in radius (R_1 , upper cavity). For broadband light, MWCNTs microcavity resonates only at low loss communication windows. Insets show magnified peaks. (c), (d) Microcavities at their resonance modes for the peaks shown in (a) and (b).

filtering in the loss communication windows. Wavelength tunability and number of resonance modes strongly depended on the number of microcavities in the arrays. Increase in the number cavities enhanced the resonant modes and produced highly intense resonance at longer wavelengths. Computational modeling has been reported for periodic MWCNT arrays to show waveguide effect and filtering at 850 and 1550 nm windows.¹⁷ An analogous effect and filtering wavelengths in these communication windows of the MWCNTs were also found from the present simulated model (Fig. 1(b) and 5). These computationally optimized MWCNT microcavities can be fabricated with PECVD method, including the in-plane Si optical waveguides.^{29–31} The light can be coupled through input port of these in-plane Si waveguides, and spectral measurements can be performed at the output port. This in-plane spectral measurements may provide measurements of the resonant modes of the MWCNT microcavities.¹⁸ Fabricated microcavities can be spectrally characterized for angle-resolved reflection measurement.¹⁸ Additionally, the diffraction properties of the fabricated device can be predicted from far-field pattern using First Fourier Transform (FFT).³² These cavities may be mass produced by using the commercially feasible techniques such as photolithography for patterning and CVD for growth. However, the minimum nanotube radius may be larger than 100 nm, which will red shift the resonances.

VI. CONCLUSION

We have demonstrated periodic MWCNT arrangements for creating microcavities with promising Q factors. MWCNT microcavities had numerous resonant modes from ultraviolet to near-infrared range, analogous to optical nano-antennas. The resonance frequencies and Q factors of the microcavities were controlled by changing MWCNT radius and cavity size. The computational model predicted resonance modes and Q factor values that allowed designing arrays with desired transmission spectra. Series and parallel MWCNT microcavity arrangement showed resonance modes that increased with cavity order. Parallel microcavities were arranged for the tunable low loss communication filter, which could be coupled with a light emitting diode (LED) source. The modeled parallel MWCNT microcavities acted as a tunable filter and showed resonance at low loss communication windows for broadband white light. We anticipate that square MWCNT microcavities may find applications in tunable filters, optical modulators, switches, and photonic integrated circuits.

¹S. Iijima, *Nature* **354**, 56 (1991).

²Z. Liu, L. Jiao, Y. Yao, X. Xian, and J. Zhang, *Adv. Mater.* **22**, 2285 (2010).

³B. Wood, J. Dyer, V. Thurgood, N. Tomlin, J. Lehman, and T.-C. Shen, *J. Appl. Phys.* **118**, 013106 (2015).

- ⁴J.-W. Zha, F. Sun, S.-J. Wang, D. Wang, X. Lin, G. Chen, and Z.-M. Dang, *J. Appl. Phys.* **116**, 134104 (2014).
- ⁵F. Wang, G. Dukovic, L. E. Brus, and T. F. Heinz, *Science* **308**, 838 (2005).
- ⁶S. M. O'Flaherty, S. V. Hold, M. E. Brennan, M. Cadek, A. Drury, J. N. Coleman, and W. J. Blau, *J. Opt. Soc. Am. B* **20**, 49 (2003).
- ⁷Z. Jin, X. Sun, G. Xu, S. H. Goh, and W. Ji, *Chem. Phys. Lett.* **318**, 505 (2000).
- ⁸E. Lidorikis and A. C. Ferrari, *ACS Nano* **3**, 1238 (2009).
- ⁹J. Sotor, G. Sobon, J. Jagiello, L. Lipinska, and K. Abramski, *J. Appl. Phys.* **117**, 133103 (2015).
- ¹⁰H. Butt, Q. Dai, T. D. Wilkinson, and G. A. Amaratunga, *Photonics Nanostruct.* **10**, 499 (2012).
- ¹¹I. Sameera, R. Bhatia, V. Prasad, and R. Menon, *J. Appl. Phys.* **111**, 044307 (2012).
- ¹²S. Uchida, A. Martinez, Y.-W. Song, T. Ishigure, and S. Yamashita, *Opt. Lett.* **34**, 3077 (2009).
- ¹³S. Kivistö, T. Hakulinen, A. Kaskela, B. Aitchison, D. P. Brown, A. G. Nasibulin, E. I. Kauppinen, A. Härkönen, and O. G. Okhotnikov, *Opt. Express* **17**, 2358 (2009).
- ¹⁴K. Chow, S. Yamashita, and S. Set, *Opt. Lett.* **35**, 2070 (2010).
- ¹⁵K. Teo, M. Chhowalla, G. Amaratunga, W. Milne, D. Hasko, G. Pirio, P. Legagneux, F. Wyczisk, and D. Pribat, *Appl. Phys. Lett.* **79**, 1534 (2001).
- ¹⁶E. Verploegen, A. J. Hart, M. De Volder, S. Tawfick, K.-K. Chia, and R. E. Cohen, *J. Appl. Phys.* **109**, 094316 (2011).
- ¹⁷H. Butt, Q. Dai, R. Rajesekharan, T. D. Wilkinson, and G. A. Amaratunga, *ACS Nano* **5**, 9138 (2011).
- ¹⁸H. Butt, A. K. Yetisen, R. Ahmed, S. H. Yun, and Q. Dai, *Appl. Phys. Lett.* **106**, 121108 (2015).
- ¹⁹H. Butt, T. D. Wilkinson, and G. A. Amaratunga, *Prog. Electromagn. Res.* **22**, 1 (2012).
- ²⁰H. Butt, Q. Dai, P. Farah, T. Butler, T. D. Wilkinson, J. J. Baumberg, and G. A. Amaratunga, *Appl. Phys. Lett.* **97**, 163102 (2010).
- ²¹F. Bommeli, L. Degiorgi, P. Wachter, W. Bacsa, W. A. de Heer, and L. Forro, *Solid State Commun.* **99**, 513 (1996).
- ²²M.-F. Lin, F.-L. Shyu, and R.-B. Chen, *Phys. Rev. B* **61**, 14114 (2000).
- ²³Q. Zhang, E. H. Hároz, Z. Jin, L. Ren, X. Wang, R. S. Arvidson, A. Lüttge, and J. Kono, *Nano Lett.* **13**, 5991 (2013).
- ²⁴A. Rifat, G. A. Mahdiraji, Y. Sua, Y. Shee, R. Ahmed, D. M. Chow, and F. M. Adikan, *IEEE Photonics Technol. Lett.* **27**, 1628 (2015).
- ²⁵A. A. Rifat, G. A. Mahdiraji, D. M. Chow, Y. G. Shee, R. Ahmed, and F. R. M. Adikan, *Sensors* **15**, 11499 (2015).
- ²⁶C. P. Tsangarides, A. K. Yetisen, F. da Cruz Vasconcellos, Y. Montelongo, M. M. Qasim, T. D. Wilkinson, C. R. Lowe, and H. Butt, *RSC Adv.* **4**, 10454 (2014).
- ²⁷A. Rifat, G. Mahdiraji, R. Ahmed, D. Chow, Y. Sua, Y. Shee, and F. Adikan, *IEEE Photonics J.* **8**, 4800408 (2016).
- ²⁸A. A. Rifat, G. A. Mahdiraji, Y. M. Sua, R. Ahmed, Y. G. Shee, and F. R. M. Adikan, *Opt. Express* **24**, 2485 (2016).
- ²⁹M. A. Bissett, A. J. Barlow, J. G. Shapter, and J. S. Quinon, *J. Appl. Phys.* **110**, 034301 (2011).
- ³⁰L. Valentini, J. Kenny, L. Lozzi, and S. Santucci, *J. Appl. Phys.* **92**, 6188 (2002).
- ³¹A. Gohier, T. Minea, M. Djouadi, and A. Granier, *J. Appl. Phys.* **101**, 054317 (2007).
- ³²H. Butt, Y. Montelongo, T. Butler, R. Rajesekharan, Q. Dai, S. G. Shiva-Reddy, T. D. Wilkinson, and G. A. Amaratunga, *Adv. Mater.* **24**, OP331 (2012).